POLITECNICO
MILANO 1863

SCUOLA DI INGEGNERIA INDUSTRIALE
E DELL'INFORMAZIONE

Executive Summary of the Thesis

Laser Powder Bed Fusion (L-PBF) Parameter Optimization for Stainless Steel 316L Porous Microlattices Printing

Laurea Magistrale in Materials Engineering and Nanotechnology

Author: Erfan Sharghivand

Advisor: Prof. Maurizio Vedani

Academic year: 2022-2023

1. Introduction

In the contemporary scientific landscape, additive manufacturing (AM) has become a focal point, attracting substantial attention from scholars and industries to dedicate extensive efforts to both AM hardware and software developments. Among the various AM methods, laser powder bed fusion (L-PBF), formerly known as selective laser melting (SLM), has undergone significant industrialization efforts, aiming for low production costs, high efficiency, and satisfactory mechanical and surface properties [5]. Particularly, L-PBF has gained attention in the realm of porous metal microlattice structure manufacturing. These structures, known for their high-performance properties such as strength-to-mass ratio, acoustic and heat insulation, and energy absorption, have become an optimal choice in various sectors like medical, aerospace, and automotive. Given the strong limitations of conventional lattice manufacturing methods and the profound impact of the L-PBF process on microstructure, porosity, and strut thickness, which collectively influence mechanical properties, the identification of optimal printing parameters is paramount [1].
This study focuses on advancing the industrialization of AM by investigating the influence of printing parameters on the mechanical properties of stainless steel 316L microlattices produced through L-PBF. The main and most effective printing parameters are shown in Figure.1.

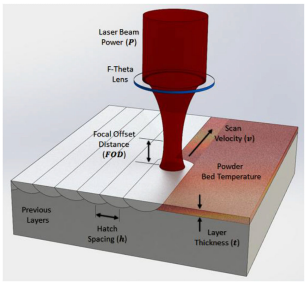

Figure 1: L-PBF Operating Parameters [2].

The correlation of the indicated parameters is highlighted through Equation.1, which is the calculation of volumetric energy density (VED) as the amount of delivered energy to the powder bed, where p is laser power, v is dedicated to scanning speed, h is hatch spacing, and t shows the thickness of the layer [2].

$$VED = E_p = \frac{p}{v \cdot h \cdot t} \quad [J/mm^3] \qquad (1)$$

Considering the characterization of the lattice structures, the compression test plays a critical role in analyzing the printed lattices and optimizing the printing parameters. As can be seen in Figure 2, there are two main compres-

sion behaviors that exist in lattice structures in bending-dominated compression: struts bend and the lattice fails in lower-yielding. However, in stretch-dominated compression, struts stretch linearly, and yielding occurs at higher stresses.

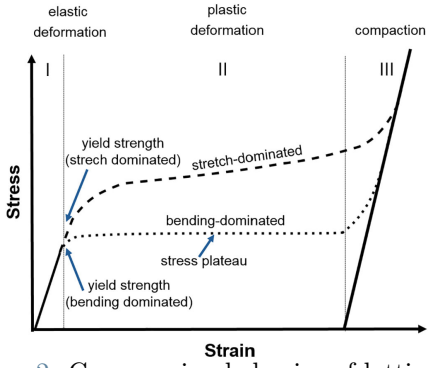

Figure 2: Compression behavior of lattice [3].

A comprehensive understanding of the main parameters, their exclusive effect on the product, and their interrelation, besides the fundamental principle of the lattice behavior under the analysis situation, provides the required knowledge for parameter optimization.

2. Materials and methods

2.1. Material

Stainless steel 316L powder with a particle size distribution (PSD) of 20 to 60 μm, is used for the studied porous lattice structures.

2.2. Samples

For this study, seven sets of stainless steel 316L square cylinder microlattices with a 100 mm^2 cross-section, as indicated in Figure 3, have been printed by the MetalOne L-PBF machine supplied by the additive manufacturing machine producer company Sharebot.

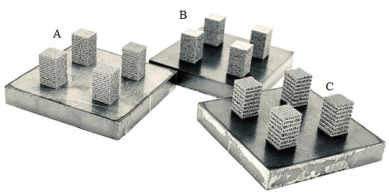

Figure 3: Delivered batches by Sharebot.

As reported in Table 1, samples were delivered in seven batches with different numbers of layers, scanning speeds, and hatch angles, while the rest of the parameters were kept constant that can be mentioned as Laser Power (p): 185W, Laser Scan (v): Continuous, Focal Length: +2 [mm], Spot Size: About 100 microns, Layer Thickness (t): 0.05 mm, Hatch Spacing (h): 400 μm.

Sample Set	Layers (#)	Hatch Angle [°]	Scan Speed [μm/s]	LED [J/mm]
A_1	10	90	600	308
A_2	10	90	550	336
A_3	10	90	500	370
B_1	5	90	600	308
B_2	5	90	550	336
B_3	5	90	500	370
C_1	10	45	600	308

Table 1: Sample Set Parameters

Additionally, the delivered energy has been calculated through Equation.2, which shows the linear energy density (LED), while p and v are the laser power and scanning speed values, respectively. The calculated delivered energy of each batch is indicated in Table 1.

$$LED = \frac{p}{v} \quad [J/mm] \tag{2}$$

Figure 4a indicates the chosen printing pattern; the hatching space has been selected to have no overlapping between the neighboring lines, so there is no hatch spacing in this setting; then the LED equation is used instead of VED (Eq. 1) for this case. As can be seen in the indicated scanning pattern in Figure 4b and reported in Table 1, apart from hatching space, different hatch angles have been applied after certain repeats of the layers to form the porous lattice structure.

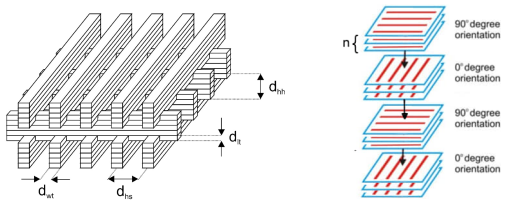

(a) (b)

Figure 4: Microlattice Scan Pattern [4].

Notably, this formation of the porous lattice structure through the selection of adjusted hatching space and hatch angle after certain repetitions is why this work diverges from the conventional use of L-PBF for lattice production and deviates from the prevalent use of CAD files.

2.3. Characterization Tests

As can be seen in Figure 3, each batch contained four identical samples, and one sample

from each batch was analyzed as-built, and the other three samples were subjected to compressive tests with different percentages and directions as follows:

1. Compressed 70% of its initial height along the Z axis or lattice building direction
2. Compressed 70% of its initial height along the X/Y axis or on the lateral surface
3. Compressed 30% of its initial height along the Z axis

Compression tests were performed with an MTS Alliance RF150 electromechanical testing machine, while each batch's last sample's compression test (30%) was coupled with the Digital Image Correlation (DIC) analysis operated by GOM Aramis 3D cameras.

The outer surfaces of all samples, as-built and compressed, were analyzed with the Zeiss EVO 50 scanning electron microscope (SEM) in the materials analysis laboratory at Politecnico di Milano. Following SEM analysis, all the samples were cut in half with Metkon's Micracut 202 automated micro cutter and then subjected to a complete metallography procedure through which a cold mounting was applied to the samples to avoid the destruction of the lattice structure under the high pressure of the hot mounting method. Subsequently, the polished cross-section and microstructure of all samples, as-built and compressed, were investigated with the light microscope before and after etching.

In order to identify the composition of the printed microlattices, an energy-dispersive spectroscopy (EDS) analysis was performed on the outer surface of the lattice.

3. Results and Discussion

3.1. EDS

The chemical composition of the printed sample was measured through the EDS test on the polished outer surface of the lattice, as given in Table 2. However, due to the EDS limitations, carbon and other light elements present in the nominal SS 316L composition were not detected.

Test	Si	Cr	Mn	Fe	Ni	Mo
1	0.95	18.01	1.37	65.26	11.97	2.44
2	0.65	17.86	1.48	64.91	12.40	2.70
3	0.68	18.22	1.51	64.76	12.28	2.55
Avg.	0.76	18.03	1.45	64.97	12.22	2.56

Table 2: Weight % of the lattice EDS results.

3.2. As-built Samples

Starting by analyzing the acquired results from the as-built lattice structures, Figure 5 represents the SEM pictures of one sample from each batch in two views from top and lateral surfaces in order to provide a vision of the differences of the understudy lattices. As can be seen in the figures, the main difference in lattice structure is caused by the varying hatch angle, where Series C is different from Series A and B. Meanwhile, the lower layer repetition caused smaller lattice pores in Series B compared to Series A.

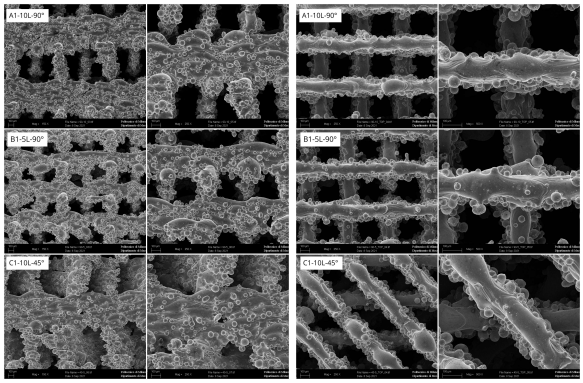

(a) (b)

Figure 5: Asbuilt SEM (a)Lateral,(b)Top view.

As can be seen, Figure 6 indicates the acquired OM results from the polished and etched cross-section of the as-built samples. The results show that Serie A samples have a more organized lattice structure with fewer detachments in the lattice structure, both between layers from the same hatch or layers from different hatches. Considering all the samples, the porosities are detectable inside the layers from the same hatch; however, the level of the priorities slightly decreased by reducing scanning speed.

Taking a close look at Figure 6 confirms the presence of two types of microstructures in all the samples, regardless of the varying parameters. Firstly, there is a granular microstructure, which can be seen mostly at the joint points of two layers from different hatches. Importantly, these regions have the same microstructure as the small balls that are attached to the main structure of the lattice and are observable in Figure 5. This microstructure, called unmelted microstructure from now on, is interpreted as the original unmelted powder, which during the printing process received enough heat to be sintered and attached together but not enough to melt and form the second present microstructure.

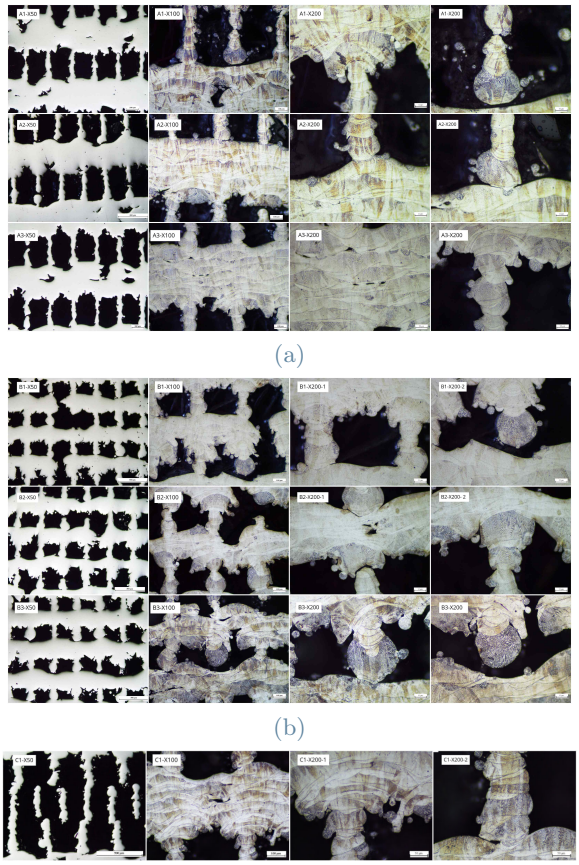

Figure 6: Asbuilt OM (a) A, (b) B, (c) C.

The second visible microstructure can be described as the granularly oriented microstructure within the perfectly melted layer-by-layer sections, where, according to the literature, the grains are elongated during the solidification step from the cold surface to the hot surface, which in this case forms along the building direction from the bottom of the melt pool to the solidified surface. The optimization of these microstructures by reducing the unmelted microstructure plays a crucial role in the resultant compressive strength since, in most cases, their interface is detected as the crack initiation point. Figure 7 represents these microstructures at high magnification. As shown in the figure, picture (1) shows the granular-oriented microstructure along the building direction, while picture (2) reveals the interface between the perfectly melted and the unmelted granular microstructure. On the other hand, picture (3) shows the importance of the melt pool penetration depth optimization, wherein inducing a proper pool depth through the control of effective printing parameters could melt the detrimental unmelted granular microstructure and form the desired perfectly granular-oriented microstructure.

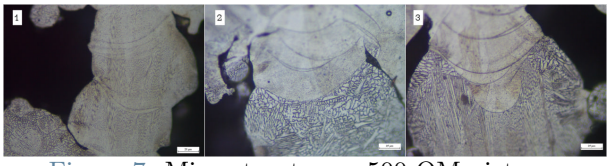

Figure 7: Microstructure, x500 OM pictures

3.3. Compressed Samples

Considering the presented results, the effect of scanning speed variation on the microstructure of the samples is negligible, so to avoid excessive data and subsequent confusion, all samples have been compressed, but only one sample from each series with a scanning speed of 600 μm/s has been subjected to the SEM and OM inspections. To have an organized report, the results are categorized based on the varying parameters.

3.3.1 Scanning Speed Effect

The stress-strain graphs for the compression tests along the Z and X/Y directions of all samples in both series A (Fig.8a) and B (Fig.8b) are presented in the given graphs. Due to the importance of the yielding stress, the initial 30% of the strain has been presented below each corresponding graph to show the yielding behavior.

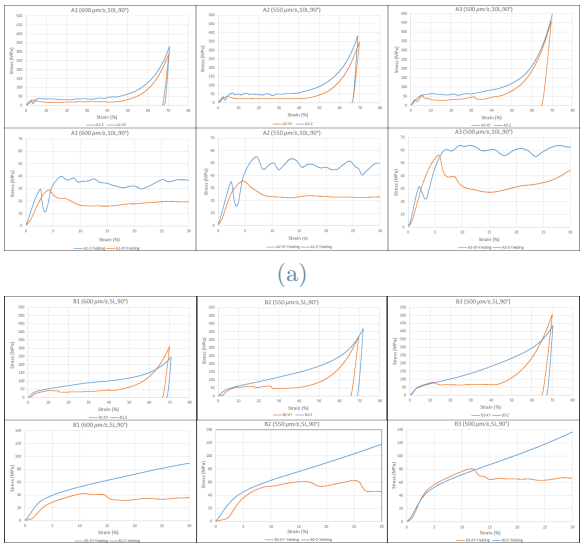

Figure 8: Stress-Strain, Scanning Speed Effect, (a) Serie A, (b) Serie B

The study of the stress-strain graphs indicates that by decreasing the scanning speed in both the A and B series, the yielding stress and maximum achieved stress increase noticeably. As indicated, Serie A samples had a bending-dominated behavior in both directions, but Serie B samples, while having similar behavior in the X/Y direction, showed a stretch-dominated behavior in compression along the Z direction.

Due to the similar behavior in the compression along the X/Y direction and the lower achieved yield stress in comparison to the compression in the Z direction, the graphs in the X/Y direction are not compared in the next categories.

3.3.2 Layer Effect

Figure 9 shows the 30 and 70% compressed A_1 and B_1 samples and confirms the presence of both previously mentioned microstructures in both structures, regardless of the layer number. The high magnification pictures clearly show that the perfectly melted joints are attached even at 70% strain, while joints with unmelted granular microstructures are simply detached and are also the main source of cracks.

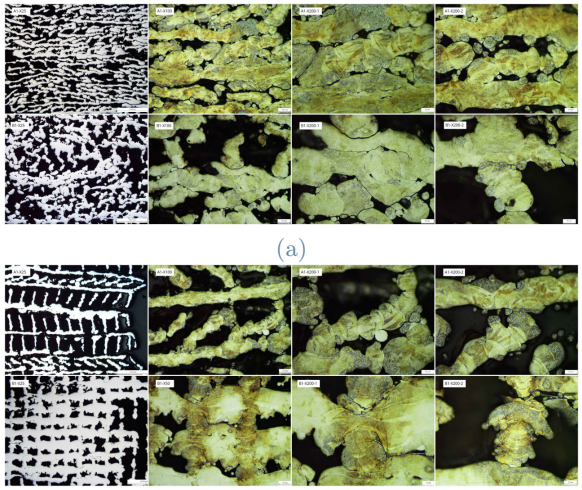

(a)

(b)

Figure 9: OM Results, Layer Effect(a)70z,(b)30z

Considering the stress-strain graphs presented in Figure 10, while both samples had similar behavior in the elastic regime, in the plastic regime, the sample with lower layers (B_1) showed stretch-dominated behavior, and the sample with a higher number of layers (A_1) showed bending-dominated behavior.

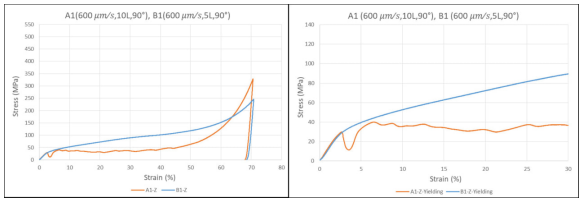

Figure 10: Stress-Strain, Layer Effect

3.3.3 Hatch Angle Effect

As shown in Figure 11, the OM pictures of the 30 and 70% compressed A_1 and C_1 samples are compared. As can be seen, both mentioned microstructures are present, but due to the higher number of joint points between layers from different hatches in sample C_1, the amount of unmelted granular microstructure in this sample is relatively higher in comparison to sample A_1. Additionally, the well-melted interface between the layers from different hatches is dramatically lower in sample C_1 compared to sample A_1.

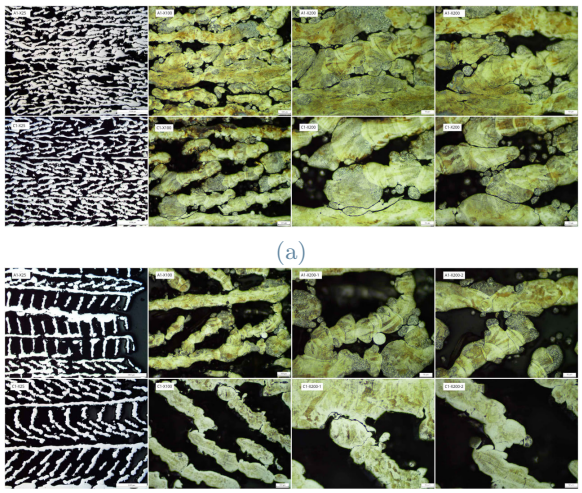

(a)

(b)

Figure 11: OM Hatch Angle Effect(a)70z,(b)30z.

All the mentioned lattice disorders in the Serie C sample led to a lower yielding stress and compaction stress compared to the lattice structure with a 90° hatch angle, which can be seen in the stress-strain graph shown in Figure 12. In addition, regardless of hatch angle, both Series C and A represent a bending-dominated behavior in response to the applied compression tests.

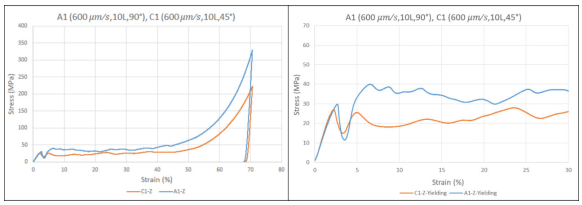

Figure 12: Stress-Strain, Hatch Angle Effect

3.4. Digital Image Correlation (DIC)

Due to the very small size of the printed microlattices and the small lattice pores, the DIC software could not detect the surface as a porous surface, so the main goal of this test, analyzing the stress and strain at the lattice points, was not fulfilled. However, through the correlation of DIC files with the stress-strain graphs, a complete confirmation of the exclusive compression behavior of each series that has been mentioned throughout this research is achieved.

The DIC results are presented as follows: Figure 13 and 15 represent the bending-dominated

compression behavior for series A and C, and Figure 14 shows the stretch-dominated compression behavior for series B samples. In each figure, the corresponding strain of every drop in stress level is highlighted with the failed layer that led to that stress relief.

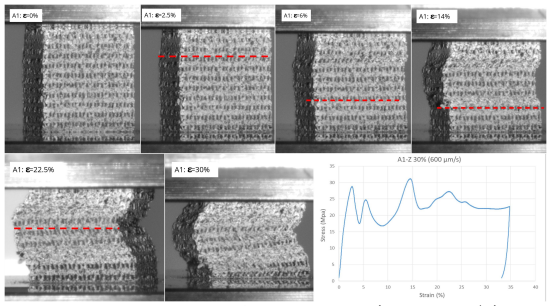

Figure 13: Serie A DIC- A_1 (600 μm/s).

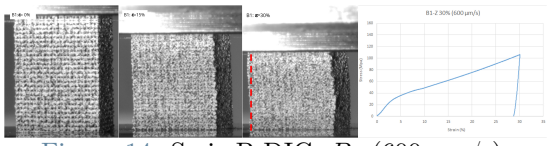

Figure 14: Serie B DIC- B_1 (600 μm/s).

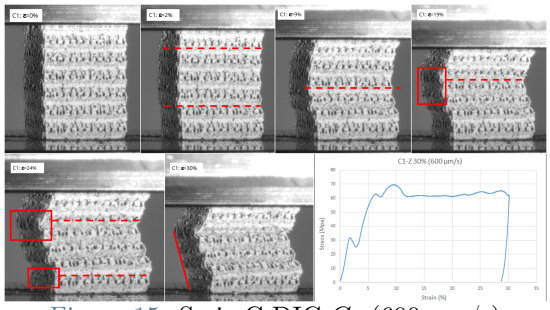

Figure 15: Serie C DIC-C_1 (600 μm/s)

4. Conclusions

This master's thesis developed over the background of additive manufacturing's fast-growing world and its influence throughout industries. The rising importance of microlattice structures in high-tech industries prompted a comprehensive study focusing on laser powder bed fusion (L-PBF) parameter optimization for fabricating stainless steel 316L porous microlattices.

Distinguishing itself from related research, this study uniquely employed the hatch angle and hatch spacing as lattice design and manufacturing means, deviating from the conventional use of CAD files. The extensive investigation of seven batches with varied parameters, utilizing scanning electron microscopy (SEM), optical microscopy (OM), and compression tests coupled with Digital Image Correlation (DIC), illuminated the interrelation between printing parameters and their effect on microstructure and compressive strength.

Results revealed quite similar microstructure but distinct failure and compression behaviors influenced by scanning speed, hatch angle, and the number of layers. Decreasing scanning speed emerged as the most impactful parameter, positively affecting compressive strength, porosity, and microstructure. Hatch angle demonstrated its significance in compressive strength and layer bonding while not affecting the microstructure. Layer number appeared as the determinative parameter for transforming stretch-dominated compression to bending-dominated compression by increasing the number of layers, causing a reduction in yield stresses. However, the compression behavior of all samples in X/Y direction compression appeared to be bending-dominated. In conclusion, the study underscores the pivotal role of a lower number of layer repetitions, reduced scanning speed, and a 90° hatch angle in optimizing mechanical properties for stainless steel 316L porous microlattices. Beyond microstructural enhancements, this parameter configuration signifies a substantial advancement in compressive strength, emphasizing the criticality of parameter optimization in L-PBF for metallic porous microlattices.

References

[1] Zefeng Xiao aet al. Evaluation of topology-optimized lattice structures manufactured via selective laser melting. *Materials Design*, 143:27–37, 2018.

[2] H. Shipley et al. Optimisation of process parameters to address fundamental challenges during selective laser melting of ti-6al-4v: A review. *International Journal of Machine Tools and Manufacture*, 128:1–20, 2018.

[3] Patrick Köhnen et al. Mechanical properties and deformation behavior of additively manufactured lattice structures of stainless steel. *Materials Design*, 145:205–217, 2018.

[4] Stamp R. et al. The development of a scanning strategy for the manufacture of porous biomaterials by selective laser melting. *T J Mater Sci*, 20:1839–1848, 06 2009.

[5] Ian et al. Gibson. *Development of Additive Manufacturing Technology*. Springer International Publishing, Cham, 2021.